NANO LETTERS

LETTER

pubs.acs.org/NanoLett

Mechanics and Dynamics of the Strain-Induced M1−M2 Structural Phase Transition in Individual VO_2 Nanowires

Hua Guo,[†,‡,#] Kai Chen,[†,‡,#] Y. Oh,[§] Kevin Wang,[†] Catherine Dejoie,[∥] S. A. Syed Asif,[§] O. L. Warren,[§] Z. W. Shan,[*,§,⊥] J. Wu,[*,†] and A. M. Minor[*,†,‡]

[†]Department of Materials Science and Engineering, University of California, Berkeley, Berkeley, California 94720, United States
[‡]National Center for Electron Microscopy, Lawrence Berkeley National Laboratory, Berkeley, California 94720, United States
[§]Hysitron, Incorporated, 10025 Valley View Road, Minneapolis, Minnesota 55344, United States
[∥]Advanced Light Source, Lawrence Berkeley National Laboratory, Berkeley, California 94720, United States
[⊥]Center for Advancing Materials Performance from the Nanoscale (CAMP-Nano), State Key Laboratory for Mechanical Behavior of Materials, Xi'an Jiaotong University, Xi'an, 710049, China

S *Supporting Information*

ABSTRACT: The elastic properties and structural phase transitions of individual VO_2 nanowires were studied using an in situ push-to-pull microelectromechanical device to realize quantitative tensile analysis in a transmission electron microscope and a synchrotron X-ray microdiffraction beamline. A plateau was detected in the stress−strain curve, signifying superelasticity of the nanowire arising from the M1−M2 structural phase transition. The transition was induced and controlled by uniaxial tension. The transition dynamics were characterized by a one-dimensionally aligned domain structure with pinning and depinning of the domain walls along the nanowire. From the stress−strain dependence the Young's moduli of the VO_2 M1 and M2 phases were estimated to be 128 ± 10 and 156 ± 10 GPa, respectively. Single pinning and depinning events of M1−M2 domain wall were observed in the superelastic regime, allowing for evaluation of the domain wall pinning potential energy. This study demonstrates a new way to investigate nanoscale mechanics and dynamics of structural phase transitions in general.

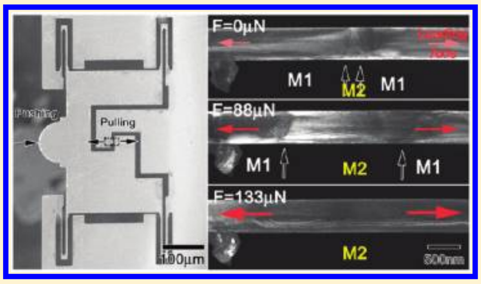

KEYWORDS: In situ, nanomechanics, VO_2, nanowires, phase transition, TEM

As a strongly correlated electron material, vanadium dioxide (VO_2) has been a model system of research for the metal−insulator transition (MIT).[1−3] Applications such as thermo/electrochromics,[4,5] Mott transistors,[6] strain sensors,[7] and thermal actuators[8] have been proposed or realized by exploiting the MIT in VO_2. The MIT occurs with a dramatic change in resistivity accompanied by a ferroelastic, structural phase transition.[3,9] The insulating, monoclinic M1 phase, which is the stable phase for undoped, strain-free VO_2 at room temperature, turns into the metallic, rutile R phase at approximately 68 °C. The MIT can be further complicated by factors such as doping[10] and strain,[11] resulting in another insulating, monoclinic phase, M2, which is metastable for undoped, strain-free VO_2. In practice, although the M1 phase is always the energetically favorable phase in free-standing VO_2 samples, small domains of M2 phase can exist when the sample is strained by a substrate.[7,12−17] According to the VO_2 strain-temperature phase diagram,[15] under tensile strain, a temperature increase results in an insulator (M1)−insulator (M2) phase transition (IIT) before the MIT (M2 to R), as shown in the phase diagram in Figure.1c. As a result, the M2 phase can be considered as an intermediate, transitional phase between the M1 and the R phase[18,19] and may play a critical role in the physics of the MIT, as well as in applications of VO_2. However, the elusive M2 phase is difficult to access and characterize due to its instability at zero or low strain states.[15] For example, its elastic properties have not been directly measured. Moreover, characterizing and differentiating the elastic and kinetic properties of these different phases are important for all device applications because all of these applications involve lattice deformation or strain, either actively or passively. For example, spontaneous strain associated with the MIT and IIT often causes cracks and fatigue in VO_2 films, which are responsible for degraded electronic transport properties; nucleation of the intermediate M2 phase, if not well calibrated, would result in large measurement error in VO_2-based strain sensors and actuators. Additionally, the domain wall pinning and depinning by bulk and surface defects would set a limit to the phase transition speed and kinetics, an effect well-known for ferroelectrics. Here we have applied a unique set of in situ mechanical testing techniques on individual VO_2 nanowires (NWs) to better understand the subtle M1 to M2 phase transition and characterize their elastic and kinetic properties, which also shed light on the phase transition mechanism of this important functional material.

Received: May 3, 2011
Revised: June 22, 2011
Published: July 07, 2011

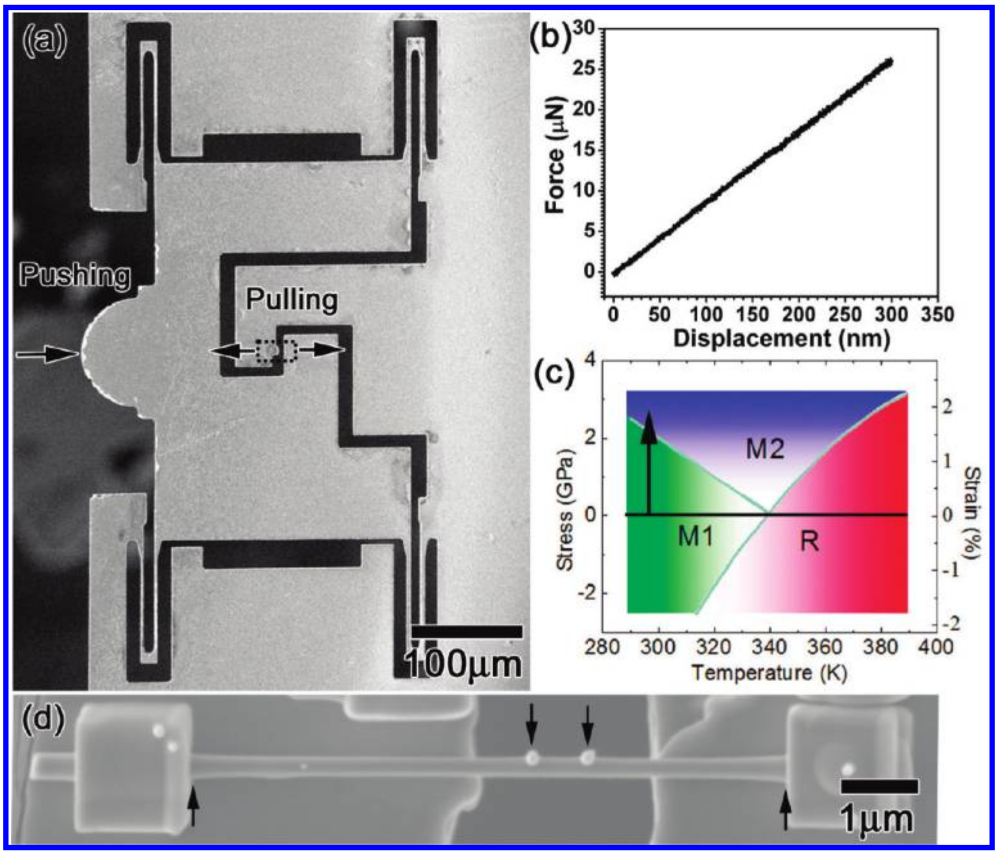

Figure 1. (a) SEM image of the microfabricated push-to-pull (PTP) device. When the device is pushed on the semicircle end (arrow at left), the specimen gap (dashed rectangle) expands while staying in the field of view of the electron microscope. (b) The linear force vs displacement response of the PTP device without a nanowire spanning the specimen gap, showing the inherent stiffness of the device. (c) The uniaxial stress (along the c_R direction)−temperature phase diagram of VO_2.[10] The arrow indicates the phase transition route under tensile loading at room temperature. (d) A higher magnification SEM image of the specimen gap of the PTP device with a VO_2 nanowire fixed across the gap by Pt welds. Two platinum dots were deposited on the sample as indicated by two arrows in the middle of the nanowire for directly measuring strain of the sample.

Experimentally, bulk VO_2 can only sustain about 0.2% elastic strain, while VO_2 NWs can routinely reach 3% and beyond.[15] Therefore, the prospect of strain inducing a phase transition in quasi-one-dimensional (1D) VO_2 nanostructures at room and/or elevated temperatures has recently attracted much attention.[7,12−17,20−22] Due to the difficulty of quantitative uniaxial strain loadings on a single NW, so far the majority of strain work has been carried out by bending the NW or passively establishing the strain via clamping.[7,12−15] In these approaches it is impossible to simultaneously achieve both the structural phase transition and direct quantitative mechanical testing. An in situ microstructural investigation of the phase transition of VO_2 has not been achieved before, and it has not been demonstrated how the domains of the new phase nucleate, grow, and propagate. To address this need, we have realized quantitative in situ tensile testing and imaging of the IIT along individual VO_2 NWs inside both a transmission electron microscope (TEM) and a synchrotron polychromatic X-ray microdiffraction (µXRD) beamline.

The VO_2 NWs used in this report were prepared using a variant of the vapor transport method which has been reported elsewhere.[14,15] The in situ tensile testing is realized by a TEM nanoindentation device (PI 95 PicoIndenter from Hysitron, Inc., Minneapolis, MN, USA)[23−26] coupled with a push-to-pull (PTP) device developed by Hysitron, Inc.[27] The PTP device is microfabricated on a silicon-on-insulator wafer and consists of a semicircular end and specifically designed cutouts, as shown in Figure 1a. When a diamond punch is driven into the semicircular end, the gap in the middle of the device is elongated and a sample spanning this gap is pulled uniaxially in tension, attenuated by the spring constant of the PTP device. The gauge section of the sample stays within the field of view of the TEM while the sample is being pulled, and a real-time video of the sample across the gap is taken. The force and displacement of the nanoindentation punch are also recorded simultaneously by the nanoindentation device. This in situ tensile testing setup allows for the investigation of the strain-induced microstructural evolution and mechanical properties in NWs and other electron-transparent samples. The force−displacement curve of an empty PTP device (i.e., without an attached test specimen) is shown in Figure 1b. As designed, the force loaded on the PTP device is linearly proportional to the motion distance of the nanoindentation punch, which represents the device stiffness along the tensile axis (about 90 N/m in this case). The linear response of the PTP device facilitates the extraction of the contribution of a sample when attached to the device, because the sample and the PTP device springs are mechanically in parallel. Therefore, what we later refer to as raw force−displacement curves include the response of the PTP device springs. The so-called raw force−displacement curves have already been corrected for the nanoindentation transducer's spring response. It should be pointed out here that the stiffness of the PTP device can be tuned by changing the dimensions of the springs and that the lateral stiffness of the PTP device is much larger than that along the tensile axis to ensure a predominantly uniaxial loading condition. Additionally, by adjustment of the stiffness or mass of the movable portion of the device, the device's resonant frequency can be improved to protect the sample from undesired sample failure during handling. A VO_2 NW was transferred to the PTP device using an Omniprobe micromanipulator in an FEI dual-beam focused ion beam (FIB)/scanning electron microscope (SEM). As shown in Figure 1d, a 270 nm wide VO_2 NW is bridging the specimen gap of the PTP device, and two platinum (Pt) patches were deposited using the FIB at the two ends of the wire to firmly bond the NW on the PTP device, resulting in a 7.8 μm long gauge length (as noted by the two outermost arrows in Figure 1d). To avoid damage caused by Ga ion irradiation by the FIB, only the parts outside of the gauge section and buried under the Pt were exposed to the ion beam during the whole process of sample preparation.

In situ TEM tensile testing of the VO_2 NWs was conducted using a JEOL 3010 TEM at 300 kV with the indenter operating in a displacement control mode at a displacement rate of 10 nm/s. Figure 2a displays a TEM bright field image of the unstrained sample. The inserted diffraction pattern can be indexed using a [122] zone axis of the M1 phase, showing that the VO_2 NW was grown along the [100] direction of the M1 phase (this was also confirmed later by the μXRD experiment). During the test the sample was loaded until sudden fracture occurred (Figure 2b), and a video of the NW behavior was recorded during the entire process (Supporting Information).

To calculate the stress on the nanowire, we measured the cross-sectional area and determined the force applied. In order to measure the cross-sectional area, the broken NW was cut using the FIB to create a surface perpendicular to the loading axis so that the true cross-sectional area could then be calculated from the projected area. The raw force—displacement curve is shown in Figure 2c. The load increased until the nanowire fractured under a force of 245 μN, noted by the arrow, and then dropped to approximately 5 μN instantaneously. As the test continued, the force increased linearly due only to the inherent stiffness of the empty PTP device, which was measured to be 30 N/m. The net force loaded on the NW was then calculated by subtracting the force contributed from the empty PTP device from the raw force.

The raw displacement data represent the motion of the diamond punch of the indenter. It includes not only the extension of the sample but also the deformation of other parts, such as the two Pt welds and the semicircular end of the PTP device where the punch is in contact. It is difficult to quantify the deformation of the welds and the semicircular end since they are both out of view in the TEM. So in order to accurately determine strain, two tiny Pt markers (as displayed in Figure 1d and Figure 2a) were deposited with the electron beam, and digital image correlation and tracking scripts using MatLab[28] were employed to allow for precise tracking of their positions. All frames of the real-time video (30 frames/s) taken during the tensile test were extracted and analyzed. The original distance and the distance change between the two fixed points on the NW were measured, and then the one-dimensional strain between the markers could be accurately determined, assuming homogeneous deformation.

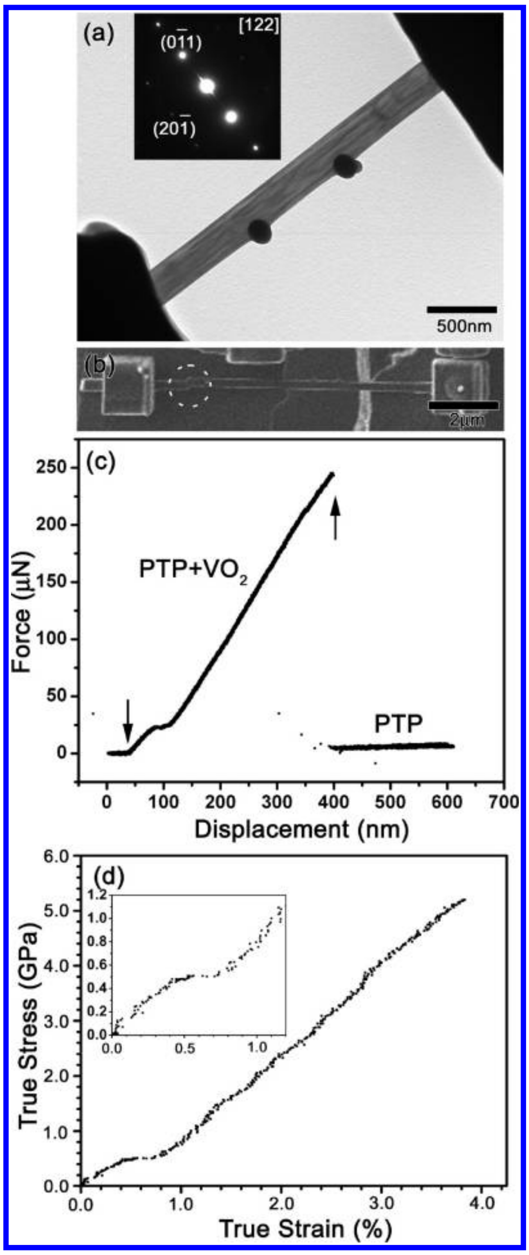

Figure 2. In situ tensile test of a VO_2 nanowire. (a) BF TEM image of a VO_2 nanowire spanning the specimen gap of the PTP device before the test, with two Pt marker dots on it. Inset is the [122] zone axis diffraction pattern indexed to the M1 phase. (b) SEM image of the fractured nanowire. The fracture location is dash-circled. (c) Raw force vs displacement curve from the in situ TEM tensile test of the VO_2 nanowire on the PTP device. The first arrow indicates the point when the diamond punch touches the semicircle end of the PTP device. During the test the wire is loaded elastically until it fractures at approximately 400 nm displacement indicated by the second arrow. (d) The resulting stress vs strain response for the VO_2 nanowire after subtraction of the linear stiffness of the empty PTP device. The inset shows a magnified view of the plateau.

A true stress—strain curve of a VO_2 NW using the method described above is shown in Figure 2d. A plateau can be clearly identified, which starts when the strain reaches about 0.48% and ends at about 0.75%. The fracture stress is about 5.2 GPa at 3.80% uniaxial tensile strain. According to the strain—temperature

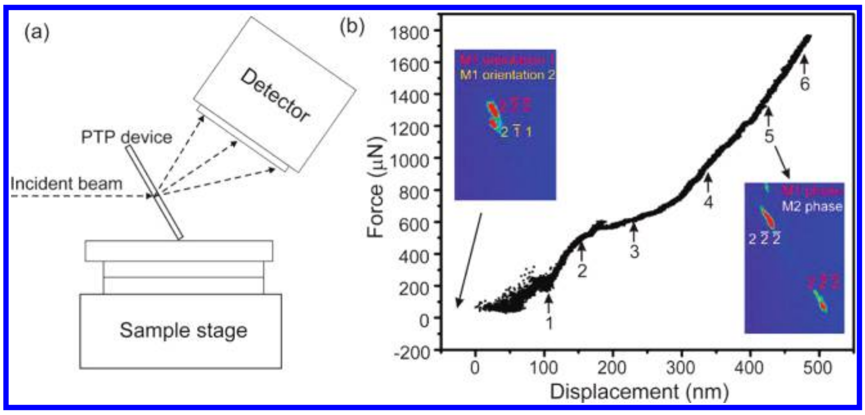

Figure 3. (a) Schematic of the microdiffraction experimental setup. (b) Raw force vs displacement curve from the in situ synchrotron X-ray microdiffraction tensile test of the VO_2 nanowire on the PTP device. The inset at the top left corner shows part of the Laue diffraction pattern taken on the VO_2 nanowire before strain loading, with Miller indices of both orientations of M1 twins, while the one at the bottom right shows the *same* area of the Laue diffraction pattern taken on the VO_2 nanowire during tensile loading at point #5 with Miller indices of both M1 and M2 phases. The drift of the absolute position of the peak $[2\overline{22}]$ in the Laue space from (c) to (d) is due to higher strain in (d).

phase diagram proposed by Cao et al,[15] the plateau then represents the superelasticity arising from the M1 to M2 phase transition under tensile loading at room temperature.[21] This is analogous to the divergent compressibility of a water−vapor coexisting system, which is a standard first-order phase transition and shares similarities with the IIT in VO_2. Therefore, if we assume that all of the M1 phase has been fully converted into the M2 phase after the plateau, the Young's moduli of the M1 and M2 structures are estimated as 128 ± 10 and 156 ± 10 GPa, respectively, based on the slope of the linear portion before and after the plateau in the stress−strain curve. These values are close to 140−155 GPa, the previously measured values of the Young's modulus of VO_2.[21,29] However, the 1D nature of the domain structure along our NW (as will be described later) and the high precision of the PTP device allowed us to estimate the Young's modulus of M1 and M2 phases for the first time. We note that any small portion of residual M1 phase after the plateau and M2 phase present before the plateau would complicate the calculation and result in error in determining their Young's moduli, as will be discussed later. Considering that the Young's modulus was reported to change by only ∼1% between the M1 and R phases in VO_2 films,[30] the difference of the Young's moduli between M1 and M2 measured in this work calls for further experimental as well as theoretical investigations.

In order to understand the microstructural phase evolution corresponding to the tensile strain, especially that associated with the plateau in the strain−stress curve, in situ μXRD experiments were conducted on Beamline 12.3.2 at the Advanced Light Source of the Lawrence Berkeley National Laboratory. A 13 μm long, 500 nm wide VO_2 NW was transferred onto a PTP device in the same way as for the TEM experiments. The in situ TEM nanoindentation holder together with the PTP device was mounted on the nanomotion stage on the beamline in transmission geometry. The VO_2 NW was aligned with a nanomotion stage, while the PTP device was tilted by about 30° back to the X-ray beam incident direction in order to prevent shadowing of the diffraction detector. A schematic of the diffraction geometry is shown in Figure 3a. The VO_2 NW was pinpointed at the focal point of the high-brilliance microfocused polychromatic synchrotron X-ray (5−24 keV) by assistance of a Keyence laser triangulation setup as well as X-ray fluorescence.[31] The X-ray beam size, which was about 1 μm × 1 μm at the focal point, was wider than the diameter of the VO_2 NW but narrower than the width of the specimen gap of the PTP device. The X-ray beam was directed orthogonal to the loading direction of the nanowire and only interacted with the gauge section of the VO_2 nanowire, confirmed by the fact that no shadowing or Si peaks from the PTP device were recorded during the experiments. A two-dimensional (2D) Pilatus X-ray detector was kept at 55° with respect to the incident X-ray beam and about 180 mm away from the sample to record Laue diffraction patterns (LPs). The geometries of the diffraction experiment, including the exact distance from the sample to the center of the detector, the tilt angles, and the center channels of the detector, were accurately calibrated by taking a Laue pattern on a strain-free Si chip. The Laue diffraction pattern showed that before any external strain loading, the VO_2 NW contained two twin orientations, both belonging to the M1 structure. A pair of diffraction peaks of both twin orientations are shown in top left inset of Figure 3b. Both orientations were aligned along the [100] direction (M1 *a* axis), which was parallel to the $(20\bar{1})$ plane normal, along the NW growth direction, and the two twin orientations were correlated by a rotation of 90.3° along the *a* axis, which was consistent with a previous report.[18] On comparison of the lattice parameters of the M1 phase that were reported by Longo et al.,[32] the lattice strain before tensile loading was derived, which proved to be almost negligible as expected. The sample was loaded in tension until the NW fractured (Figure 3b). Seven LPs were taken with 8 s exposures each, six of which were before fracture and are marked in Figure 3b. With all the LPs indexed, the phase and lattice strain distribution were analyzed. It was found that only the twinned M1 phase was observed at low strain levels when LP #1 and #2 were taken, while the M2 phase started to appear at the plateau of the curve, when simultaneously the intensity of the M1 diffraction peaks becomes weaker. This confirms that the plateau indeed corresponds to the ferroelastic M1−M2 phase transition. The [010] direction, which is also the (010) plane normal, of the M2 phase was indexed to be parallel to the *a* axis of the M1 phase as well as the NW direction. Interestingly, a small signal of the M1 phase persisted and coexisted with the M2 phase even after the plateau until fracture, as demonstrated by LP #5 in the bottom right inset of Figure 3b. The lattice strain at #5 was derived to be

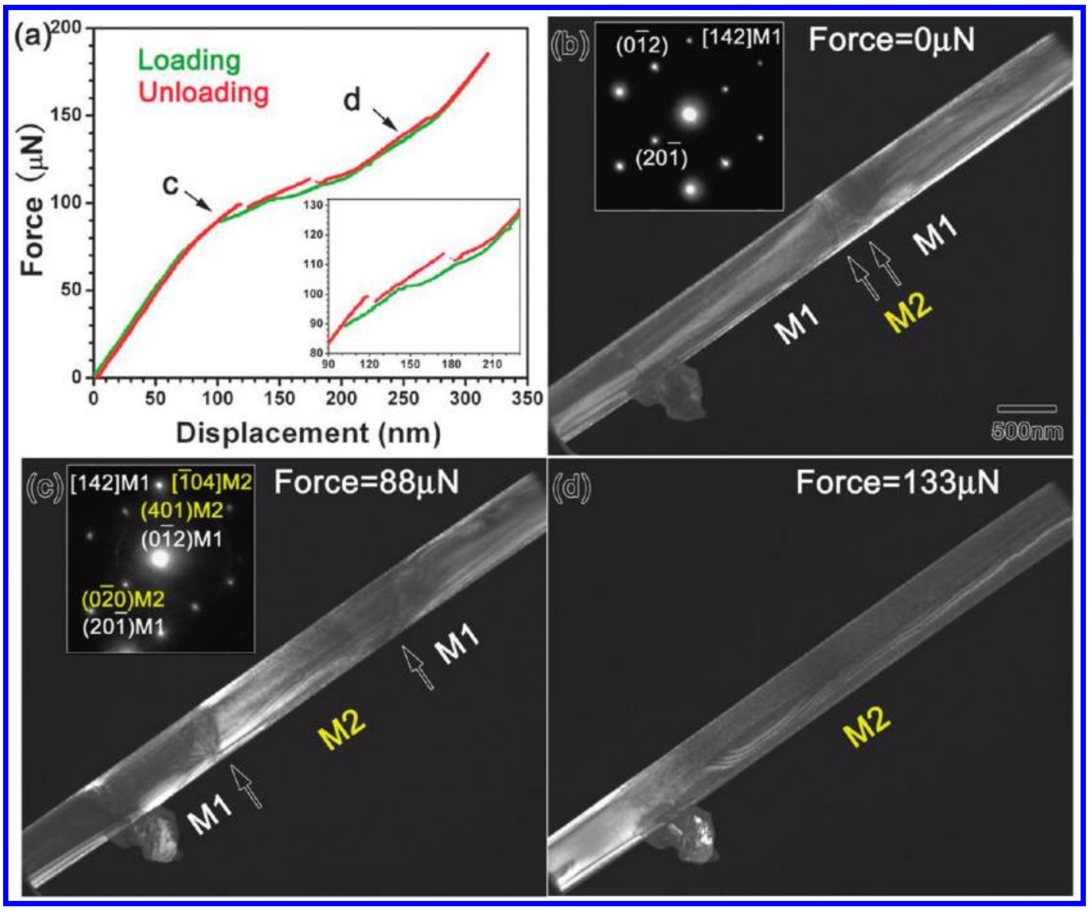

Figure 4. (a) Raw force vs displacement curve from an in situ TEM tensile test of a VO_2 nanowire on the PTP device during loading (in green) and unloading (in red). (b) DF TEM images of the unstrained VO_2 nanowire. (c) Sample at loading of 88 μN and (d) sample at loading of 133 μN. Diffraction pattern of M1 phase in a zone axis of [142] in inset of (b) is almost the same as the one of M2 phase in a zone axis of [$\bar{1}$04] in inset of (c). As the loading increased, the walls separating M1 and M2 phases (indicated by the arrows) moved in opposite directions, reflecting the expansion of the M2 domain.

about 2% from the position of the M2 diffraction peaks as compared to the strain-free lattice parameters reported by McWhan et al.,[33] which is slightly smaller than but consistent with the macroscopic strain estimated from the raw force−displacement curve. The integrated intensity of the diffraction peaks from the M2 phase was over 10 times higher than the intensity of M1 peaks, indicating that about 90% of the material had turned to M2 phase. Thus, the error bars for our calculation of the moduli of the two phases include the possibility of 10% residual M1 phase in the presumed M2 single phase region. The LP taken after fracture was almost identical to the one taken before strain loading, proving that the system reverted to the M1 phase in the strain-free state.

To investigate how the M2 phase nucleates, grows, and propagates, several cycles of loading and unloading were applied in the TEM. According to the raw force−displacement curve in Figure 4a, the initiation and completion of the plateau in the curve occurred at 80 and 155 μN, respectively, with the response of the PTP device included. Figure 4b shows that after several strain loading/unloading cycles, a small M2 domain (between the two arrows) was stabilized along the NW at room temperature even without external strain loading. Considering the large stress needed for the M2 phase to be stable, it is possible that the NW has some residual tensile strain from the sample preparation process[14,15] or the assembling process,[7] as suggested in previous reports. It is likely that this M2 domain is sandwiched between two initial M1 twins, because the M1 twin wall is expected to be the lowest-energy location for a new phase to nucleate.[34] As the tension on the NW increased (Figure 4b), the M2 domain was seen expanding in both directions. Panels c and d of Figure 4 show the image at a force of 88 and 133 μN, respectively. During the phase transition process, the domain walls shift uniaxially along the NW axis, and the propagation velocity of the two M1−M2 domain walls was dependent on the strain rate of the sample. While the M2 domain expands, the NW maintains the M1/M2/M1 structure, and no new M1 domains nucleate elsewhere; this suggests that the M1−M2 domain wall is the preferred nucleation position for the growth of a new M2 phase out of the M1 phase. This is expected because bonds are distorted across the M1−M2 domain wall and thus there is a positive interface energy associated with the wall; as such, the system would prefer to minimize the M1−M2 domain wall area during the tensile test, hence forming a one-dimensionally aligned domain chain with the smallest number of domains. It is interesting to note the different speeds of the two M1−M2 domain walls in Figure.4, even though they are subjected to the same uniaxial stress. This may be caused by different crystal orientations of these two walls, which set different nucleation barrier heights for the M1-to-M2 transition.

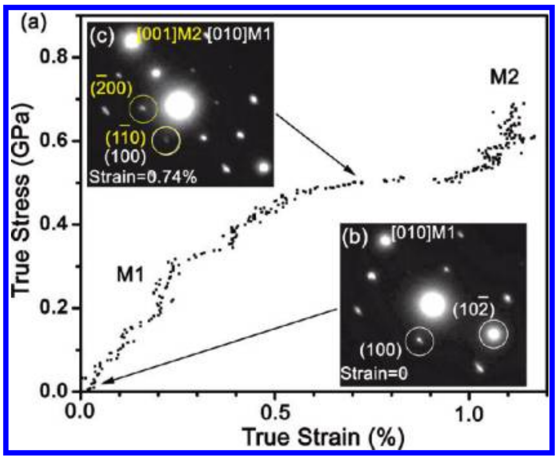

Figure 5. (a) True stress vs true strain curve from an in situ TEM tensile test of a VO_2 nanowire on the PTP device during loading. (b) Diffraction pattern of the unstrained VO_2 nanowire and (c) diffraction pattern at the start of the plateau at strain of 0.74%. The strain-induced M2 phase can be clearly distinguished in the [001] zone axis as compared to the original [010] M1 phase.

The diffraction patterns of the M1 and strain-induced M2 phases are shown in the insets of panels b and d of Figure 3, respectively. No noticeable change could be found in the diffraction patterns between the M1 phase in the zone axis of [142] and the M2 phase in the zone axis of $[\bar{1}04]$, which is consistent with the TEM observation by Sohn et al.[22] However, when a nanowire is aligned to the [010] zone axis of M1 during testing, the strain-induced M2 phase that emerges in the [100] zone axis can be clearly distinguished via electron diffraction patterns, as shown in Figure 5.

It is interesting to note that there exist minijumps in the force−displacement curve especially near the plateau, as shown in Figure.4a. Comparing to the real-time video of the domain wall drift, it is clear that these minijumps are correlated to single depinning events of the M1−M2 domain wall during the wall motion. The wall is pinned most likely by bulk or surface defects, because the domain wall energy would be lowered at these defects.[35,36] The energy potential required to depin the trapped domain wall is an important parameter that fundamentally limits the phase transition kinetics when a large number of domains are present in the specimen.[37] This pinning potential can be estimated from the integrated area enclosed by the mini hysteresis loop in the force−displacement curve at each individual pinning event. From Figure.4a the pinning energy density is estimated to be on the order of ∼100 mJ/m^2, which is larger than the energy density of static M1−R domain walls (25 mJ/m^2).[12] This large pinning potential may be due to some strong pinning defects on the surface of the VO_2 NW such as surface nonstoichiometry or surface roughness.

In summary, the strain-induced structural phase transition in VO_2 NWs was investigated with in situ TEM and synchrotron μXRD. A plateau in the stress−strain curve was observed and could be attributed to the superelasticity of the M1−M2 phase transition. The elastic moduli of these two phases were differentiated and the threshold strain for the transition was directly determined. In situ μXRD data suggest the existence of a small amount of residual M1 phase even in the elastic regime at high tensile strain. In situ TEM observations demonstrate that preexisting M2 phase acts as an initiation site during the process of M2 phase expansion. The M1−M2 domain wall motion is uniaxial, and reversible but the motion dynamics show pinning and depinning events of the individual domain walls. We expect that this in situ push-to-pull TEM testing method can be utilized to probe the nanoscale phase transition dynamics for a wide range of functional materials such as ferroelectrics and shape memory alloys.

■ ASSOCIATED CONTENT

Ⓢ Supporting Information. A video showing nanowire behavior. This material is available free of charge via the Internet at http://pubs.acs.org.

■ AUTHOR INFORMATION

Corresponding Author

*E-mail: zhiweishan@gmail.com, wuj@berkeley.edu, aminor@berkeley.edu.

Author Contributions

#These authors contributed equally to the work.

■ ACKNOWLEDGMENT

The authors acknowledge that the research was supported in part by a US Department of Energy SBIR Grant (DE-FG02-07ER84813) awarded to Hysitron, which does not constitute an endorsement by DOE of the views expressed in the article. The microdiffraction program at the ALS on BL 12.3.2 was made possible by NSF Grant No. 0416243. The in situ experiments were performed at the National Center for Electron Microscopy and the Advanced Light Source at the Lawrence Berkeley National Laboratory, which is supported by the Office of Science, Office of Basic Energy Sciences, Scientific User Facilities Division, of the U.S. Department of Energy under Contract No. DE-AC02—05CH11231. Z. W. Shan was supported by NSFC (50925104) and the 973 program of China (2010CB631003). Materials synthesis (J.W.) was supported by an NSF CAREER Award under Grant Number DMR-1055938.

■ REFERENCES

(1) Morin, F. J. *Phys. Rev. Lett.* **1959**, *3*, 34–36.

(2) Mott, N. F. *Rev. Mod. Phys.* **1968**, *40*, 677.

(3) Eyert, V. *Ann. Phys. (Berlin)* **2002**, *11*, 650–704.

(4) Manning, T. D.; Parkin, I. P.; Pemble, M. E.; Sheel, D.; Vernardou, D. *Chem. Mater.* **2004**, *16*, 744–749.

(5) Rakotoniaina, J. C.; Mokrani-Tamellin, R.; Gavarri, J. R.; Vacquier, G.; Casalot, A.; Calvarin, G. *J. Solid State Chem.* **1993**, *103* 81–94.

(6) Kim, H. T.; Chae, B. G.; Youn, D. H.; Maeng, S. L.; Kim, G.; Kang, K. Y.; Lim, Y.-S. *New J. Phys.* **2004**, *6*, 52.

(7) Hu, B.; Ding, Y.; Chen, W.; Kulkarni, D.; Shen, Y.; Tsukruk, V. V.; Wang, Z. L. *Adv. Mater.* **2010**, *22*, 5134–5139.

(8) Cao, J.; Fan, W.; Zhou, Q.; Sheu, E.; Liu, A.; Barrett, C.; Wu, J. *J. Appl. Phys.* **2010**, *108*, 083538.

(9) Berglund, C. N.; Guggenheim, H. J. *Phys. Rev.* **1969**, *185*, 1022.

(10) Pouget, J. P.; Launois, H.; D'Haenens, J. P.; Merenda, P.; Rice, T. M. *Phys. Rev. Lett.* **1975**, *35*, 873.

(11) Marezio, M.; McWhan, D. B.; Remeika, J. P.; Dernier, P. D. *Phys. Rev. B* **1972**, *5*, 2541.

(12) Wu, J.; Gu, Q.; Guiton, B. S.; de Leon, N. P.; Ouyang, L.; Park, H. *Nano Lett.* **2006**, *6*, 2313–2317.

(13) Wei, J.; Wang, Z.; Chen, W.; Cobden, D. H. *Nat. Nanotechnol.* **2009**, *4*, 420–424.

(14) Cao, J.; Ertekin, E.; Srinivasan, V.; Fan, W.; Huang, S.; Zheng, H.; Yim., J. W. L.; Khanal, D. R.; Ogletree, D. F.; Grossman, J. C.; Wu, J. *Nat. Nanotechnol.* **2009**, *4*, 732–737.

(15) Cao, J.; Gu, Y.; Fan, W.; Chen, L. Q.; Ogletree, D. F.; Chen, K.; Tamura, N.; Kunz, M.; Barrett, C.; Seidel, J.; Wu, J. *Nano Lett.* **2010**, *10*, 2667–2673.

(16) Zhang, S.; ChouJ., Y.; Lauhon, L. J. *Nano Lett.* **2009**, *9* 4527–4532.

(17) Jones, A. C.; Berweger, S.; Wei, J.; Cobden, D.; Raschke, M. B. *Nano Lett.* **2010**, *10*, 1574–1581.

(18) Mun, B. S.; Chen, K.; Leem, Y.; Dejoie, C.; Tamura, N.; Kunz, M.; Liu, Z.; Grass, M. E.; Park, C.; Yoon, J.; Lee, Y. Y.; Ju, H. *Phys. Status Solidi: RRL* **2011**, 107–109.

(19) Tselev, A.; Luk'yanchuk, I. A.; Ivanov, I. N.; Budai, J. D.; Tischler, J. Z.; Strelcov, E.; Kolmakov, A.; Kalinin, S. V. *Nano Lett.* **2010**, *10*, 4409–4416.

(20) Sohn, J. I.; Joo, H. J.; Porter, A. E.; Choi, C. J.; Kim, K.; Kang., D. J.; Welland, M. E. *Nano Lett.* **2007**, *7*, 1570–1574.

(21) Fan, W.; Huang, S.; Cao, J.; Ertekin, E.; Barrett, C.; Khanal, D. R.; Grossman, J. C.; Wu, J. *Phys. Rev. B* **2009**, *80*, 241105.

(22) Sohn, J. I.; Joo, H. J.; Ahn, D.; Lee, H. H.; Porter, A. E.; Kim, K.; Kang, D. J. M.; Welland, E. *Nano Lett.* **2009**, *9*, 3392–3397.

(23) Minor, A. M.; Asif, S. A. S.; Shan, Z. W.; Stach, E. A.; Cyrankowski, E.; Wyrobek, T. J.; Warren, O. L. *Nat. Mater.* **2006**, *5*, 697–702.

(24) Warren, O. L.; Shan, Z. W.; Asif, S. A. S.; Stach, E. A.; Morris, J. W.; Minor, A. M. *Mater. Today* **2007**, *10*, 59–60.

(25) Shan, Z. W.; Mishra, R. K.; Asif, S. A. S.; Warren, O. L.; Minor, A. M. *Nat. Mater.* **2008**, *7*, 115–119.

(26) Shan, Z. W.; Adesso, G.; Cabot, A.; Sherburne, M. P.; Asif, S. A. S.; Warren, O. L.; Chrzan, D. C.; Minor, A. M.; Alivisatos, A. P. *Nat. Mater.* **2008**, *7*, 947–952.

(27) Oh, Y.; Cyrankowski, E.; Shan, Z. W.; Asif, S. A. S. Micro/Nano-Mechanical Test System Employing Tensile Test Holder with Push-to-Pull Transformer USA Patent Application number 20100095780.

(28) Eberl, C.; Gianola, D. S.; Thompson, R. *MatLab Central*; The Mathworks, Inc.: Natick, MA, 2006), File ID:12413.

(29) Tsai, K. Y.; Chin, T. S.; Shieh, H. P. D. *Jpn. J. Appl. Phys.* **2004**, *43*, 6268.

(30) Sepulveda, N.; Rua, A.; Cabrera, R.; Fernandez, F. *Appl. Phys. Lett.* **2008**, *92*, 191913.

(31) Martin, K.; Nobumichi, T.; Kai, C.; Alastair, A. M.; Richard, S. C.; Matthew, M. C.; Sirine, F.; Edward, E. D.; James, M. G.; Jonathan, L. K.; Gregory, Y. M.; Dave, W. P.; Brian, V. S.; Tony, W.; Valeriy, V. Y.; Howard., A. P.; Ersan, U. *Rev. Sci. Instrum.* **2009**, *80*, 035108.

(32) Longo, J. M.; Kierjegaard, P. *Acta Chem. Scand.* **1970**, 24.

(33) McWhan, D. B.; Marezio, M.; Remeika, J. P.; Dernier, P. D. *Phys. Rev. B* **1974**, *10*, 490.

(34) Tselev, A.; Meunier, V.; Strelcov, E.; Shelton, W. A.; Luk'yanchuk, I. A.; Jones, K.; Proksch, R.; Kolmakov, A.; Kalinin, S. V. *ACS Nano* **2010**, *4*, 4412–4419.

(35) Lee, W. T.; Salje, E. K. H.; Bismayer, U. *Phys. Rev. B* **2005**, *72*, 104116.

(36) Lee, W. T.; Salje, E. K. H.; Goncalves-Ferreira, L.; Daraktchiev, M.; Bismayer, U. *Phys. Rev. B* **2006**, *73*, 214110.

(37) Salje, E. K. H. *Phase Transitions in Ferroelastic and Co-Elastic Crystals: An Introduction for Mineralogists, Material Scientists, and Physicists*; Cambridge University Press: Cambridge, 1990.